Investigating the Uncertainty Contribution of the NF/FF Transformation Processing for Electrically Large Antennas

Francesco Saccardi[1], FELLOW AMTA, Stephane Issartel[2], Nicolas Gross[2], Lars J. Foged[1], FELLOW AMTA
(1) MVG, MICROWAVE VISION GROUP, Pomezia, Italy
(2) MVG, MICROWAVE VISION GROUP, Villejust, France

***Abstract*— This paper examines the uncertainty contributions associated with the spherical Near-Field to Far-Field (NF/FF) transformation process when applied to electrically large antennas. The transformation is based on the Spherical Wave Expansion (SWE) and implemented through the Transmission Formula (TXF), which provides a mathematically rigorous and computationally efficient framework. The TXF supports multiple levels of Probe Correction (PC), each with varying complexity and accuracy. However, applying the TXF to electrically large antennas (e.g. larger than 500 wavelengths) present significant computational challenges. The large number of spherical harmonics required increases the processing burden, and the accurate evaluation of the rotation and translation operators becomes critical. These operators must be computed using suitable recurrence relations to avoid instabilities. Additionally, the use of probes with arbitrary patterns can further complicate the probe correction process, potentially introducing numerical instabilities that must be carefully controlled. This work investigates the accuracy of the NF/FF transformation for electrically large antennas by considering both idealized cases without PC, and more realistic scenarios with full PC. The ability to compensate for large tapering effect introduced by the probe will be addressed for the first time.**

***Index Terms*—full probe correction, spherical near field, spherical wave expansion, transmission formula.**

I. INTRODUCTION

The predecessor of MVG, SATIMO, was founded in 1986. In 1992, SATIMO introduced its first commercial multi-probe system, a Spherical Near-Field (SNF) measurement solution now known as the StarGate (SG) and StarLab (SL) systems [1]. The system's revolutionary speed enabled rapid design cycles and iterative testing, capabilities that were otherwise not feasible with either measurement or numerical simulation tools available at the time.

With hundreds of SG and SL systems sold worldwide, MVG has sustained a dedicated internal development effort from the outset to continuously enhance its Near-Field to Far-Field (NF/FF) transformation software and associated post-processing capabilities [2]. The initial NF/FF software was based on the formulation known in Hansen's book [3].

During the early development and customer acceptance phases, MVG's NF/FF was rigorously validated for numerical accuracy, computational speed, and angular resolution. Benchmarking was performed against leading commercial implementations already in use by early customers [4].

Due to the high-speed nature of SG system measurements, users routinely acquired data at hundreds of frequencies, making post-processing efficiency a critical factor. The MVG NF/FF transformation code development was aimed at ensuring that data processing would not be a bottleneck in overall system performance. The original MVG NF/FF transformation software, named *SatSph*, was written entirely in Fortran, the most suitable scientific computing language at the time. In subsequent years, several advanced post-processing features including diagnostic back-propagation and truncation error mitigation [5], were introduced and packaged into a dedicated module called *SatMap*.

Leveraging the significantly enhanced computational efficiency of MATLAB [6], the Spherical Wave Expansion (SWE) and its associated Transmission Formula (TXF) were re-implemented in MATLAB in 2012. This milestone enabled the development of a broad and continuously evolving suite of tools. Among these are *MvSphere*, MVG's current NF/FF transformation software, and *MvEcho*, a spatial filtering tool based on SWE and translation operations, designed to mitigate the impact of imperfect RF environments in near-field measurements [7].

Alongside software development, MVG has also driven continuous innovation in probe design, supporting both multi-probe arrays and traditional single-probe scanning systems. These efforts aimed to push the boundaries of achievable bandwidth and measurement fidelity [8], [9]. The emergence of wideband probe requirements and large scan angles led to the development of higher-order probe compensation methods [10]-[12], currently available within *MvSphere*.

Moreover, the need to test offset AUTs, common in applications such as automotive and space, led to the development of the Translated Spherical Wave Expansion (TSWE) method [13], [14]. TSWE allows arbitrary repositioning of the reference coordinate system within the SNF measurement range, thereby reducing required sampling while maintaining accuracy.

Further capabilities were added in response to evolving application needs. For example, in the automotive sector, the *AnyGround* tool was introduced to handle ground planes made

of various materials [15], and algorithms were developed to remove reflections caused by conductive surfaces [16].

In parallel, MVG invested significantly in the development of advanced diagnostic techniques based on equivalent current expansion [17]. These methods provide deep insight into the behavior of antennas under test (AUTs) and serve as a crucial link between accurate measurements and numerical simulation workflows [18].

The scientific software suite available at MVG is highly versatile, and its modular architecture enables efficient customization and the development of internal tools. These tools are particularly valuable for advanced analysis of measurement systems, including fast generation of detailed system uncertainty budgets [19] .

In this paper, we examine the accuracy of the NF/FF transformation as currently implemented in *MvSphere* when applied to electrically large antennas (exceeding 500 wavelengths in size) which require extremely dense sampling, on the order of 0.1° or finer [20]. The analysis focuses on the uncertainty introduced by the transformation process, comparing two approaches: the simplified SWE-TXF formulation without probe correction, and the more computationally intensive method incorporating full probe correction.

II. SWE-Based NF/FF Transformations

The most widely adopted method for performing the spherical NF/FF transformation is based on the SWE [3]. In this approach, the measured SNF data are first projected onto a set of Spherical Wave Functions (SWF), yielding the corresponding Spherical Wave Coefficients (SWC). The SWC are then combined with the SWF evaluated at an infinite distance to complete the transformation to FF.

A more specific and well-known implementation involves the use of the Transmission Formula (TXF), as shown in (1), which leverages the Fourier properties of the SWE and enables probe correction (PC) by de-embedding the influence of the measurement probe.

$$w(r,\theta,\varphi,\chi) = \sum_{\substack{smn \\ \sigma\mu\nu}} Q^{(4)}_{smn} e^{jm\varphi} d^n_{\mu m}(\theta) e^{j\mu\chi} R_{\sigma\mu\nu} C^{sn}_{\sigma\mu\nu}(kr) \quad (1)$$

The TXF expresses the complex signal received by a probe (w) of known coefficients ($R_{\sigma\mu\nu}$) as a function of the probes spherical coordinates (r,θ,φ) and orientation (χ) when an Antenna/Device Under Test (AUT/DUT), described by its own spherical wave coefficient ($Q^{(4)}_{smn}$) transmits. The symbols $d^n_{\mu m}(\theta)$ and $C^{sn}_{\sigma\mu\nu}(kr)$are respectively rotation and translation operators that, together with the two complex exponentials ($e^{jm\varphi}$ and $e^{j\mu\chi}$), are used to describe the probe position/orientation in each measurement point. The rotation and translation operators are the most critical components of the TXF, as their correct implementation is essential for ensuring both numerical stability and computational efficiency.

The rotation operator plays a key role in enabling the use of the Fast Fourier Transform (FFT) along the θ-coordinates. This is achieved by expressing the rotation coefficients as a Fourier series using the so-called delta-pyramid coefficients, as detailed in appendix A2 of [3] and shown in (2). To maintain numerical stability at high mode indices (e.g. $n > 1000$), different recurrence relations are employed [3].

$$d^n_{\mu m}(\theta) = i^{m-\mu} \sum_{m'} \Delta^n_{m'\mu} \Delta^n_{m'm} e^{im'\theta} \quad (2)$$

The translation operator is used to compute the probe response constant (PRC), which depends on the scanning distance, r , and the SWC of the probe, as shown in (3). Evaluating the PRC is non-trivial, as it involves complex mathematical constructs such as binomial coefficients and Wigner 3-j symbols, as detailed on appendix A3 of [3]. If not carefully implemented, the evaluation of the PRC can lead to divergences and impact the accuracy of the probe correction.

$$P_{s\mu n}(kr) = \sum_{\sigma\nu} R_{\sigma\mu\nu} C^{sn}_{\sigma\mu\nu}(kr) \quad (3)$$

As discussed in [11], the TXF supports multiple levels of probe correction, including First Order PC (FOPC), single-polarized and dual-polarized full PC. The inversion of the TXF varies significantly depending on the PC applied [10]-[12].

In some measurement scenarios, such as when using an electrically small probe and/or when the scanning distance is relatively large compared to the DUT size, the probe effect can be neglected. In such cases, the probe is modeled as a Hertzian dipole, simplifying the TXF inversion and allowing FFT to be applied along both scanning axes. In the First-Order Probe Correction (FOPC) approach, only the $\mu = \pm 1$ modes of the probe are considered. This still permits FFT usage along both scanning axes but may introduce residual errors if the probe is not of first-order type.

To overcome these limitations, full probe correction techniques have been developed [10]-[12]. These allow greater flexibility in probe selection without compromising the measurement accuracy, as the probe's influence is fully compensated during the transformation. This is particularly advantageous when using wideband probes (e.g., with bandwidths of 15:1 or more), enabling faster measurement acquisitions [11]. However, this comes at the cost of increased computational complexity. In fact, the NF/FF transformation now requires matrix inversion along the θ-axis, with the FFT applied only along the φ-axis [10], [12] . Moreover, full PC enables further generalization, such as accounting for different radiation patterns in dual-polarized probes, whereas FOPC assumes identical radiation patterns from both probe ports [3].

It is also important to note that highly directive probes can negatively impact the numerical stability of the transformation. This is due to the tapering effect, which reduces the dynamic range and can degrade the condition number of the matrix used in the inversion process. This paper will evaluate the accuracy of full probe corrected NF/FF transformations in the context of electrically large AUTs and varying degrees of tapering introduced by different probe types.

III. SWE Analysis without Probe Correction

In this initial investigation, we evaluate the uncertainty introduced by applying the NF/FF transformation in a measurement scenario where probe correction is not required. Due to the simplicity PRC in this case, here the focus is basically primarily on assessing the accuracy of the rotation coefficient computation within the TXF when dealing with electrically large DUT.

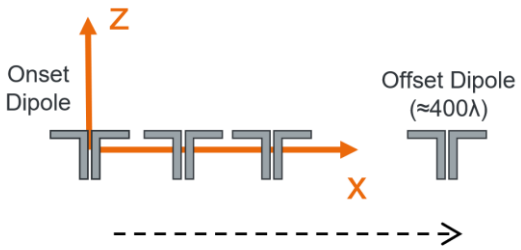

Figure 1. Simulated SWE scenario with Hertzian dipole with increasing offset.

The numerical measurement setup, illustrated in Figure 1, is inspired by the approach in [21]. A Hertzian dipole is used as AUT, and its position is incrementally offset along the x-axis from the origin of the coordinate system. Translations from 0 up to more than 400λ are considered. For each displacement, the far-field radiation pattern is computed at an infinite distance.

The radiation patterns are sampled according to standard guidelines based on the radius of the minimum sphere enclosing the AUT, centered at the coordinate origin [21]. An additional 10% on the number of samples has been considered to better observe the behavior of the high order modes, not associated with the antenna, which should ideally exhibit zero-power. In particular, the radiation pattern of the furthest-offset dipole is sampled with an angular resolution of approximately 0.06° in both θ and φ, resulting in a maximum mode index of N = 2957, corresponding to a DUT diameter of 941λ.

To assess the transformation accuracy, the SWC are computed from the defined radiation patterns inverting the TXF (without probe correction). The FF pattern is then reconstructed on the same angular grid (i.e., FF/FF transformation), and the input and output patterns are compared using the Equivalent Noise Level (ENL) metric, defined in (4):

$$ENL = 20\log_{10}\left(RMS\left|\frac{E(\theta,\varphi)_R - E(\theta,\varphi)_T}{E(\theta,\varphi)_{R,MAX}}\right|\right) \qquad (4)$$

where RMS denotes the root mean square operator, and $E(\theta,\varphi)_R$ and $E(\theta,\varphi)_T$ represent the reference and test radiation patterns, respectively.

To establish a baseline for the ENL, Gaussian random noise with a signal-to-noise ratio (SNR) of 200 dB is added to each input pattern. In the absence of transformation errors, the ENL should ideally match the negative SNR value (i.e., ENL = –SNR), providing a clear threshold for evaluating transformation fidelity.

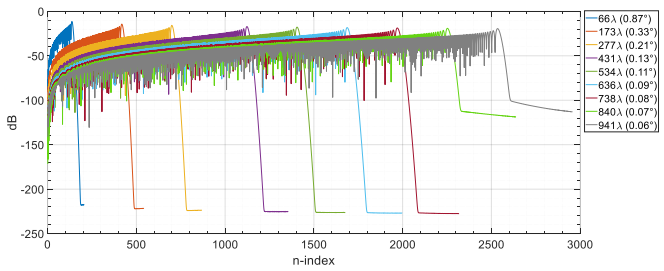

Figure 2. Computed Pn power spectra from the SWE of radiation pattern with different sampling density.

The computed SWC are presented in terms of the normalized Pn-power spectra defined in [21]. These results are shown in Figure 2 for each test case scenario. The corresponding input sampling parameters and the equivalent maximum DUT size are indicated in the figure legend.

As expected, the peak of each trace is found at the mode index corresponding to the antenna's offset. Beyond this point, the SWC values decay consistently with the expectation [3], [21]. The observable plateau is due to the 10% margin considered on sampling of the input pattern. For most test cases, this plateau lies approximately 200dB below the peak, aligning well with the 200dB SNR used in the input data. However, in the two scenarios with the largest offsets, the plateau level is noticeably elevated. As also observed in [21] , this behavior is a consequence of finite numerical precision in the input data. Specifically, the standard double-precision [6] is insufficient to accurately represent the rapidly varying phase of a highly offset source with a residual error better than -200dB, leading to an elevated numerical noise floor. Although the plateau remains below the noise floor of typical measurement systems, it could be further reduced by increasing the numerical precision of the input data.

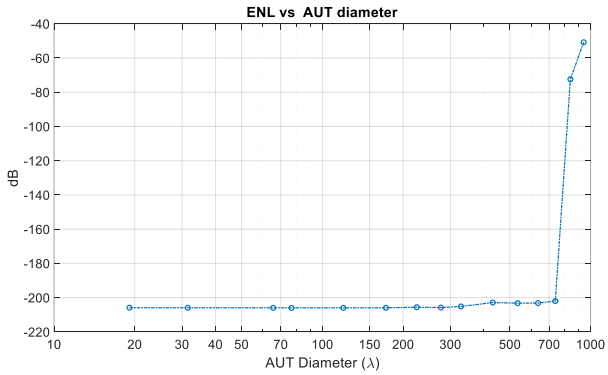

Figure 3. ENL obtained for the different test cases with varying antenna offset (i.e. AUT equivalent diameter).

Figure 3 presents the ENL, computed using (4), for the various test cases involving increasing antenna offsets, which correspond to larger equivalent AUT diameters and denser angular sampling. For antennas with diameters up to approximately 700λ, the ENL remains below the –200 dB threshold, consistent with the SNR assumed in the input data.

The fact that the ENL falls below the noise floor is attributed to the processing gain inherent in the transformation process [22].

It is important to note that these excellent results were achieved using standard double numerical precision for AUT diameters up to 431λ, corresponding to a sampling interval of approx. 0.13°. For larger AUTs, requiring finer sampling intervals, local increases in numerical precision were applied in the most critical part of the code, particularly in the computation of the delta coefficients used in the rotation operator (2).

As shown in the figure, a significant rise in ENL (up to –50 dB) is observed in the two test cases with the largest offsets. This behavior mirrors the elevated plateau seen in the corresponding Pn-spectra and is again attributed to the limitations of double numerical precision of the input data. Specifically, the rapid phase variations introduced by large offsets cannot be accurately represented with the same residual error as in the other test cases. This conclusion was validated by repeating the tests with the same fine sampling intervals (0.07° and 0.06°) but with reduced AUT offsets. In these cases, the expected –200 dB residual error was successfully recovered.

Further analysis (not shown here for brevity) focused on the rotation operator implementation shows that, in theory, the current algorithm can support SWE up to mode indices of N=9000, equivalent to a 0.02° sampling interval or a maximum AUT diameter of nearly 3000λ. However, the numerical precision of the input data becomes a critical limiting factor at such scales. Additionally, in practical measurement scenarios, the precision of the measurement system itself must be considered, as it must support such dense angular sampling with sufficient accuracy.

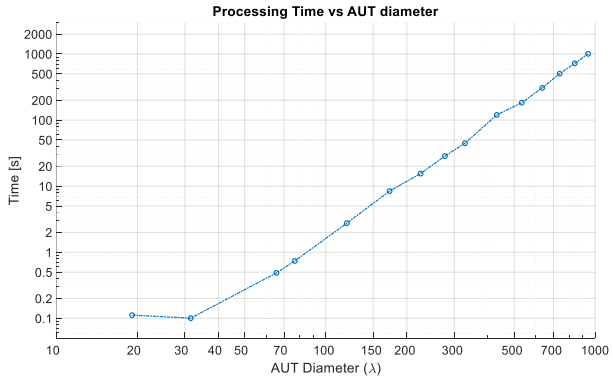

Figure 4. SWE (w/o PC) processing time varying the AUT diameter (laptop equipped with an Intel(R) Core(TM) Ultra7 155H, 3800MHz processor and 32GB RAM).

Figure 4 illustrates the SWE processing time for each test case. The computations were performed on a standard laptop equipped with an Intel® Core™ Ultra 7 155H 3800MHz. Using a logarithmic scale on both axes, the plot shows the expected exponential growth in processing time with increasing problem size. Notably, even for electrically large AUTs, up to 200λ in diameter, the transformation can be completed in just a few seconds, highlighting the efficiency of the implementation.

IV. SWE Analysis with Full Probe Correction

In the second part of this investigation, the NF/FF transformation with full, dual-polarized probe correction is analyzed. To evaluate its performance and limitations, a set of realistic emulated measurement scenarios has been considered. As illustrated in Figure 5, the setup consists of a SNF system with a 7-meter scanning radius. High-fidelity full-wave simulations were used to model both the AUT and the probe. Specifically, the AUT is a wideband horn antenna (SH1000 by MVG, operating from 1 to 18 GHz), while the probe is a dual-polarized quad-ridge horn (QH4000 by MVG, operating from 4 to 40 GHz). For brevity, the analysis is limited to five frequency points: 6, 9, 12, 15, and 18 GHz.

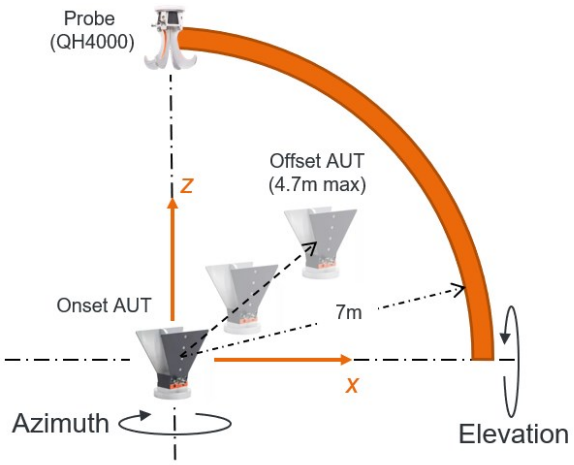

Figure 5. Sketch of the emulated measurement scenario.

To rigorously test the NF/FF transformation, the AUT is progressively displaced from the center of the measurement system, thereby increasing the electrical size of the problem and amplifying the field tapering effects introduced by the probe. It is well known that such probe-induced effect become more pronounced as the AUT is moved away from the system center or, equivalently, as the AUT size increases. In this study, the AUT is diagonally offset along the x, y, and z axes, with total displacements ranging from 0 to approximately 4.7m. Given the AUT's minimum radius of 30 cm, this corresponds to a maximum equivalent DUT diameter of 10 meters. Relative to the 7m scanning radius, this configuration represents a challenging scenario, with a worst-case field of view of approx. ±45°.

To better understand the tapering effect introduced by the probe in this geometry, the normalized electric field radiated by the probe within the 10-meter Test Zone (TZ) is computed and shown in Figure 6 for 6, 12, 15, and 18 GHz. In these plots, the TZ is centered at the origin, while the probe is located at (x, y, z) = (0, 0, –7) m. The 2D field cuts represent the H-plane of the probe, which exhibits the strongest tapering. As expected, the Test Zone Taper (TZT) increases with frequency and becomes more significant near the edges of the TZ.

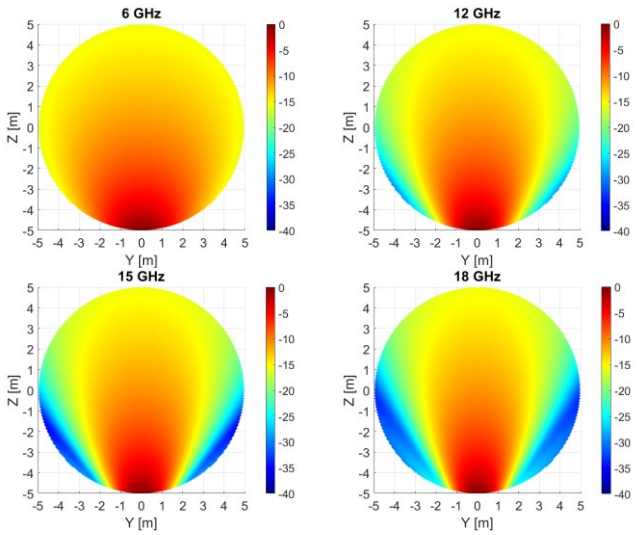

Figure 6. Test zone illumination provided the probe (H-plane).

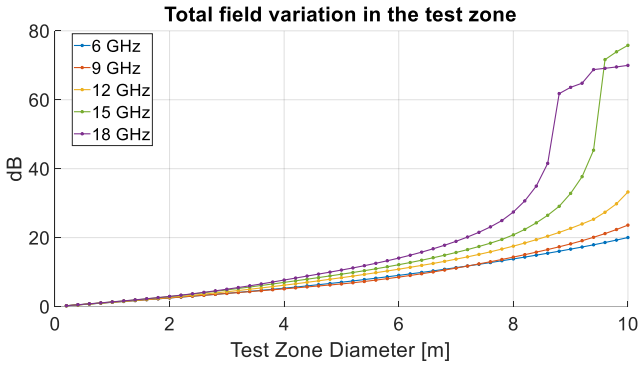

Figure 7. TZT provided by the probe for different test zone size and frequencies.

Figure 7 presents the total TZT, computed over the full 3D test zone, as a function of both frequency and TZ size. This chart provides insight into the expected effectiveness of the probe correction. For instance, at 15 and 18 GHz, the TZT exceeds 70 dB for a 10-meter TZ, implying that a SNR significantly better than 70 dB is required for effective compensation. However, if the TZ (or equivalently, the DUT size) is reduced to 8 meters, the TZT drops to 20 dB at 15 GHz and 27 dB at 18 GHz, thereby relaxing the SNR requirements.

In this analysis, random noise was added to the simulated SNF data to achieve a SNR of 80 dB. As in the previous section, the accuracy of the full PC NF/FF transformation is evaluated using the ENL defined in (4), where the reference pattern is the known far-field of the AUT, and the test pattern is the result of the transformation including full PC.

Figure 8 presents the ENL patterns, computed using (4) before applying the RMS operator, for various antenna displacements. The solid traces correspond to results obtained using the dual-polarized full PC. The residual error floor at -80dB, introduced by the simulated noise, is clearly visible. In the main beam region, a slight larger residual error is observed for larger antenna offsets. This is due to the increasing tapering effect introduced by the probe, reaching nearly 40dB when the AUT is offset by 4m. The dashed trace represents the result for the 4m offset case without applying probe correction. The significantly higher ENL in this case highlights the importance of accounting for the probe pattern in such scenarios.

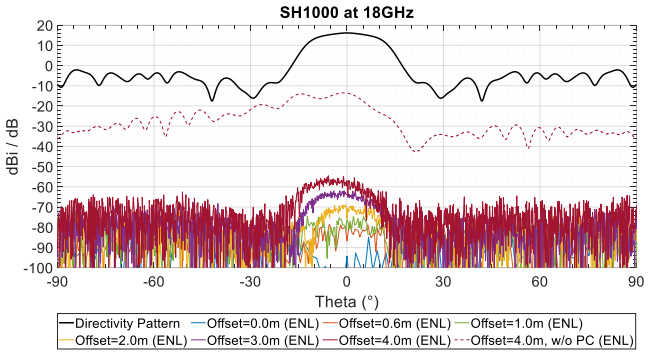

Figure 8. Reference radiation pattern at 18GHz and associated ENL for different antenna displacements.

	AUT / Test Zone Diameter						
	0.6m	1.8m	2.5m	4.5m	6.5m	8.5m	10.0m
6 GHz	ENL=-86dB TZT=0.7dB	ENL=-86dB TZT=2.2dB	ENL=85dB TZT=3.2dB	ENL=-84dB TZT=6.3dB	ENL=-82dB TZT=10.3dB	ENL=-79dB TZT=15.2dB	ENL=-76dB TZT=20.0dB
9 GHz	ENL=-86dB TZT=0.7dB	ENL=-86dB TZT=2.2dB	ENL=-85dB TZT=3.2dB	ENL=-84dB TZT=5.9dB	ENL=-82dB TZT=10.0dB	ENL=-80dB TZT=16.1dB	ENL=-75dB TZT=23.6dB
12 GHz	ENL=-86dB TZT=0.7dB	ENL=-86dB TZT=2.3dB	ENL=-85dB TZT=3.6dB	ENL=-84dB TZT=7.5dB	ENL=-82dB TZT=12.5dB	ENL=-80dB TZT=20.0dB	ENL=-73dB TZT=33.2dB
15 GHz	ENL=-86dB TZT=0.8dB	ENL=-85dB TZT=2.6dB	ENL=-85dB TZT=3.9dB	ENL=-84dB TZT=8.2dB	ENL=-82dB TZT=13.8dB	ENL=-78dB TZT=25.0dB	ENL=-13dB TZT=76.2dB
18 GHz	ENL=-86dB TZT=0.8dB	ENL=-85dB TZT=2.6dB	ENL=-84dB TZT=4.0dB	ENL=-80dB TZT=9.2dB	ENL=-76dB TZT=16.3dB	ENL=-71dB TZT=37.4dB	ENL=-14dB TZT=75.2dB

Figure 9. Achived ENL for each test configuration and comparison with the test zone taper (TZP) provided by the probe.

Figure 9 summarizes the ENL results for all test cases, alongside the corresponding TZT introduced by the probe. A clear correlation between TZT and the resulting ENL is observed. In most cases (green cells), the ENL remains consistent with the introduced 80dB SNR, indicating effective compensation. In these scenarios, the total TZT does not exceed 25 dB, and is almost entirely mitigated during the transformation (only a slight increase in ENL is observed as TZT grows). When the TZT reaches approximately 33–37 dB, a moderate increase in ENL is observed (yellow cells), though the compensation remains highly effective. As expected, the full PC begins to fail only when the TZT approaches the SNR introduced in the simulation.

These results clearly demonstrate the robustness of the full PC approach, even for electrically large antennas (up to over 600λ in diameter in this study). The few degraded cases are attributed to the strong tapering effect of the probe, which cannot be fully compensated given the SNR limitations. In such situations, it is advisable to use a probe with reduced taper, to maintain the same test zone size while preserving transformation accuracy.

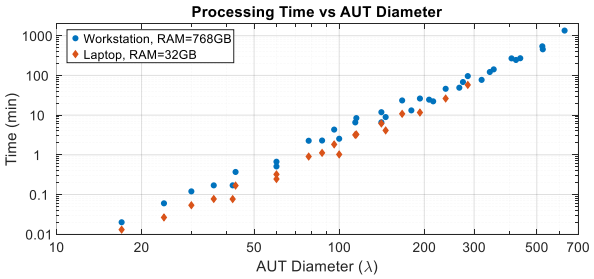

Figure 10. Processing time of the dual-pol. full PC: workstation with Intel(R) Xeon(R) Gold 6230CPU @2.10GHz processor and 768GB RAM (blue); same laptop used in Figure 4 (orange).

Figure 10 shows the processing time for dual-polarized full PC across the considered test cases, categorized by the AUT electrical diameter. Compared to Figure 4, the increased processing time is due to the added complexity of the dual-polarized full PC. For AUT sizes up to approx. 300λ, the same laptop used in previous tests was considered. Notably, even such large problems can be handled on a modern laptop with 32GB of RAM, achieving computation times on the order of a few minutes for DUTs up to approx. 100λ. However, for larger cases, the current implementation required a workstation with significantly more memory. While the increase in processing time is substantial, it scales well with the expected behavior. Ongoing code optimizations aim to improve computational efficiency for these electrically large scenarios.

V. CONCLUSIONS

In this paper a detailed investigation into the uncertainty contribution of the spherical NF/FF transformation when applied to electrically large antennas is reported.

The paper has examined the accuracy of the NF/FF transformation in two distinct scenarios. First, under idealized conditions without probe correction, the transformation was shown to be highly accurate for antennas up to 700λ, with residual errors at larger sizes primarily due to limitations in numerical precision of the input data. Second, in realistic measurement scenarios involving full probe correction, the study confirms that transformation accuracy is preserved. However, the tapering effect introduced by the probe must be carefully addressed to avoid degrading the signal-to-noise ratio, which could compromise the effectiveness of the correction.

Finally, the paper evaluates the computational performance of the transformation process. Despite the added complexity of full probe correction, antennas up to 100λ in diameter can be processed in few minutes with the current implementation. Instead, when probe correction can be omitted, electrically large DUTs, up to 200λ in diameter, the transformation can be completed in just a few seconds.

Overall, the study confirms the robustness and scalability of the SWE-based NF/FF transformation, whose contribution to typical measurement system uncertainty budgets can be considered negligible, even in the case of electrically large antennas.

REFERENCES

[1] P. O. Iversen, P. Garreau and D. Burrell, "Real-time spherical near-field handset antenna measurements," in IEEE Antennas and Propagation Magazine, vol. 43, no. 3, pp. 90-94, June 2001

[2] IEEE Std 1720-2012 "Recommended Practice for Near-Field Antenna Measurements"

[3] J. E. Hansen (ed.), Spherical Near-Field Antenna Measurements, Peter Peregrinus Ltd., on behalf of IEE, London, United Kingdom, 1988

[4] https://www.ticra.com/software/snift/

[5] L. J. Foged, L. Duchesne, Ph. Garreau, P.O. Iversen, J-Ch. Bolomey, "Truncation impact on measured radiation pattern in spherical near field antenna test ranges", IEEE APS Symposium and USNC-URSI National Radio Science Meeting, July 8-12, 2001, Boston, USA.

[6] https://www.mathworks.com/

[7] L. J. Foged et al., "Echo Suppression by Spatial Filtering Techniques in Advanced Planar and Spherical NF antenna Measurements", 34th Annual Symposium of the Antenna Measurement Techniques Association, AMTA, October 2012, Seattle, Washington, USA

[8] L. J. Foged, L. Duchesne, L.Roux, Ph. Garreau, "Wide-band dual polarized probes for high precision near-field measurements", AMTA 2002, 3-8 November, Cleveland Ohio.

[9] L. J. Foged, A. Giacomini, L. Duchesne, C. Feat, "Wide-band dual polarized probes for near field antenna measurements" AMTA 2006, October 22-27, Austin TX.

[10] F. Saccardi, A. Giacomini, L. J. Foged, "Probe Correction Technique of Arbitrary Order for High Accuracy Spherical Near Field Antenna Measurements", AMTA 2016, October 30 – November 4, Austin, TX, USA

[11] F. Saccardi, A. Giacomini, L. J. Foged, T. Blin "Experimental Validation of Full Probe Correction Technique using Wideband and Dual-Polarized Probes in Spherical NF Antenna Measurements" AMTA 2021, October 24-29, Daytona Beach, FL, USA

[12] Tommi Laitinen, et al. "Theory and Practice of the FFT/Matrix Inversion Technique for Probe-Corrected Spherical Near-Field Antenna Measurements With High-Order Probes", IEEE TAP, Vol. 58, No.8, August 2010

[13] F. Saccardi, F. Rossi, F. Mioc, L. J. Foged, P.O. Iversen, "Application of the Translated-SWE Algorithm for the Characterization of Antennas Installed on Cars Using a Minimum Number of Samples", AMTA 2017, 15-20 October, Atlanta, GA, USA

[14] F. Saccardi, N. Gross, G. Vincenzi and L. J. Foged, "Spherical Near Field Measurements of Electrically Large Offset Antennas with Minimum Sampling," EuCAP 2023, Florence, Italy, 2023

[15] F. Saccardi, F. Mioc, A. Giacomini, L. J. Foged, "Estimation of the Realistic Ground Effect in Free-Space Automotive Measurements", AMTA 2018, 4-9 November, Williamsburg, Williamsburg, VA, USA

[16] F. Saccardi et al., "Comparative Investigation of Spatial Filtering Techniques for Ground Plane Removal in PEC-Based Automotive Measurements," AMTA 2019, 6-11 Oct. 2019, San Diego, CA, USA

[17] M. A. Francavilla, J. L. Araque Q., G. Vecchi, A. Giacomini, L.J. Foged, "Antenna diagnostics for low and medium directivity antennas based on the equivalent current approach", AMTA 2009, Salt Lake City, UT, US

[18] L. J. Foged et al., "The Missing Link between Numerical Simulation and Antenna Measurements with Application to Flush Mounted Antennas," AMTA 2014, October 2014, Tucson, Arizona, USA

[19] F. Saccardi, A. Giacomini, L. J. Foged "Accurate Evaluation of Antenna Measurement Range Performance with the SWE Transmission Formula" AMTA 2023, October 8-13, Seattle, WA, USA

[20] https://5gaa.org/content/uploads/2024/04/5gaa-wg3-vatm-technical-report.pdf

[21] F. Jensen, A. Frandsen "On the Number of Modes in Spherical Wave Expansions" AMTA 2004, Stone Mountain Park, GA, USA

[22] L. J. Foged, M. Faliero, P. O. Iversen, "Random noise in spherical near field systems", AMTA 2009, Salt Lake City, Utah, November 2009.